Extreme Mechanics Letters 36 (2020) 100670

Contents lists available at ScienceDirect

Extreme Mechanics Letters

journal homepage: www.elsevier.com/locate/eml

Transformation from 2D meta-pixel to 3D meta-pixel using auxetic kirigami for programmable multifunctional electromagnetic response

Dinh Hai Le [a], Ying Xu [a], Manos M. Tentzeris [b], Sungjoon Lim [a,*]

[a] School of Electrical and Electronic Engineering, Chung-Ang University, Heukseok-Dong, Dongjak-Gu, Seoul, 06974, Republic of Korea
[b] School of Electrical and Computer Engineering, Georgia Institute of Technology, 85 5th St NW, Atlanta, 30308 GA, USA

ARTICLE INFO

Article history:
Received 30 January 2020
Received in revised form 9 March 2020
Accepted 12 March 2020
Available online 14 March 2020

Keywords:
Metamaterials
Kirigami
Coding
Multifunctional metamaterial
Metamaterial absorber

ABSTRACT

Implementation of multiple functions on the metamaterials can greatly broaden their potential application. Origami-based metamaterials, whose buck properties can be manipulated by tuning the specific folding angle, have currently become a supplemental method for conventional reconfigurable metadevices. Approaching kirigami with transformable features and idea of a functional metastructure, this paper numerically and experimentally investigates a multifunctional electromagnetic response with mechanically programmable characteristic based on an auxetic kirigami pattern in gigahertz frequency regime. The metamaterial unit cell has 2-dimensional (2D) five meta pixels. Each 2D meta-pixel can be transformed to the 3-dimensional (3D) meta-pixel and it is coded by ternary number (-1, 0, +1) for different folding levels. The kirigami pattern provides five transformable tessellations corresponding to five distinct functions of electromagnetic reflector, band-pass filter and polarization-selectable absorbers. The performance of the proposed programmable multifunctional metamaterial is numerically and experimentally demonstrated. This study can motivate the realization of kirigami computing, code-driven multifunctional metastructures.

1. Introduction

Metamaterials are well known as a class of artificially engineered materials that normally have a 2-dimension (2D) periodic arrangement [1,2]. Due to the extraordinary electromagnetic (EM) properties such as negative refraction [3], induced transparency [4], and reversed Cherenkov radiation [5], with various operating frequency from Hz to visible ranges [6–11], metamaterials have been widely applied in many fields consisting of medicine [12], energy [13], environment [14], and mechanical engineering [15,16], etc.

With the dramatic development of advanced systems and devices, functional metamaterials have currently become an important research area. Digital programming [17–20], electrical control [21–23], reconfigurable shaped-changing [24,25], and other external stimuli [26–28] have been employed to obtain multiple EM behaviors of metamaterials. In recent investigations, origami and kirigami applications in engineering have been developed, providing important insights for functional electro-mechanic metamaterial research. Origami and kirigami are the traditional Japanese art of cutting ("kiri" means cut) and/or folding paper, transforming 2D flat sheets into complex 3-dimensional (3D) structures. These techniques offer promising approaches to control mechanical [29,30], acoustic [31], and EM properties [32–35], through reconfigurable functionalities and multistability due to shape changes and simple tailoring of topology characteristics, respectively. For example, Mura origami can be used to achieve tunable chirality [32] and frequency selective surface [33]; whereas, kirigami brings interesting results of flexural wave control [34] and reconfigurable toroidal circular dichroism [35]. However, most reported metastructures have common restrictions in number of functions, high cost and structural complexity.

In this paper, a multifunctional metamaterial is investigated using the codable auxetic kirigami structure which can be mechanically programmed by selecting kirigami patterns with different Poisson's ratio, as illustrated in Fig. 1. It is demonstrated that the proposed metamaterial can provide multifunctional electromagnetic response of full reflection, frequency-selective transmission and polarization-selective absorption by transforming the 2D meta-pixel to the 3D meta-pixel. For instance, at Mode I, it is working as band-pass filter with a center frequency f_1. At Mode II, it is working as a reflector. At Mode III, it is working as an electromagnetic (EM) absorber at frequency f_0 and its polarization can be selected. At Mode III-1, it can absorb only transverse electric (TE) polarized EM wave while it absorbs only transverse magnetic (TM) polarized EM wave at Mode III-2. At Mode III-3, it absorbs both TE and TM wave, where absorption frequency and

* Corresponding author.
E-mail address: sungjoon@cau.ac.kr (S. Lim).

https://doi.org/10.1016/j.eml.2020.100670
2352-4316/

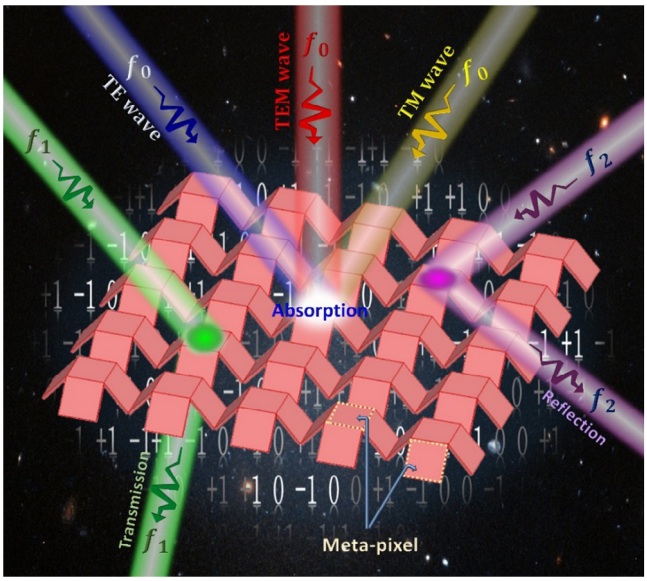

Fig. 1. Conceptual illustration a multifunctional metamaterial. A single metamaterial can realize five distinct functionalities by changing folding state of an auxetic kirigami structure. f_0 and f_1 denote the absorption and band-pass frequencies, whereas f_2 represents the entire frequency range.

ratio can be changed by varying the folding angle at Mode III-3. Furthermore, EM responses according to continuously minor and major changes of folding angle are studied to support absorption and band-pass properties. The performance of the proposed multifunctional metamaterial will be numerically and experimentally demonstrated.

2. Materials and methods

2.1. Kirigami pattern: Geometry and mechanical properties

Fig. 2 shows the proposed kirigami pattern geometries for four folded tessellations from flat sheet. The propose kirigami sheet has one central meta-pixel defined by facet lattice constant a, and four symmetrically 2D meta-pixel defined by folding length h and folding width a. The kirigami pattern is cut from flat sheet paper and transformed to various 3D shapes by mechanically programming values of α and β. It is noted that the kirigami unit cell in Fig. 2b and c, Fig. 2d and e are correspondingly symmetric in (x, y) plane. Hence, for more concrete view about kirigami pattern, Fig. 2f and g exhibit detailed geometries for two representative unit cells with structural parameters by folding four edge meta pixels in up and down states. As can be seen in Fig. 2f, all edge meta pixels are down, i.e., both α and β range from 0° to 90°. For the second unit cell, two opposite meta-pixel elements are going up, whereas two remaining meta pixels are going down, i.e., α and β range from 0° to 90° and 0° to −90°, respectively. The unit cell shown in Fig. 2f applies to the tessellations in Fig. 2b and c, whereas Fig. 2g applies to the tessellations in Fig. 2d and e (see Figure S1). The kirigami unit cell heights, y_α and y_β, width, w, and length, l, change with changing α and β. We defined overall length, width, and height along the x, y, and z axes respectively,

$$\begin{aligned} & y_\alpha = h.\sin\ |\alpha|\,,\ y_\beta = h.\sin\ |\beta|\,, \\ & l = a + 2h.\cos\ \alpha,\ w = a + 2h.\cos\ \beta, \\ \text{and}\quad & y = y_\alpha + y_\beta = |h.\sin\ \alpha| + |h.\sin\ \beta|\,; \end{aligned} \tag{1}$$

where y is the total height of the second unit cell (see Fig. 2g).

Poisson's ratio is the ratio of transverse contraction strain to longitudinal extension strain in the direction of stretching force [36,37]. Since most buck materials become thinner in the cross section in stretch showing the positive Poisson's ratio, the negative Poisson's ratio (auxetic materials) with potential applications have been receiving more attentions [38–40]. Due to the changeable capacity and easy transformation between mode and mode, the Poisson's ratio of the proposed kirigami pattern is numerically investigated. Fig. 2h shows calculated results of the linearized planar Poisson's ratio of both unit cell in Fig. 2f and g, which are defined as:

$$\vartheta_{lw} = -\frac{\frac{dl}{l}}{\frac{dw}{w}} = -\frac{\sin|\alpha|\,(a + 2h.\cos\beta)}{\sin|\beta|\,(a + 2h.\cos\alpha)} \tag{2}$$

Since the linearized planar Poisson's ratios (in (x, y) plane) are equal at both unit cells in Fig. 2f and g, for all folded patterns, the proposed kirigami produces an auxetic metamaterial with negative Poisson's ratio. In the case $\alpha = \beta$, $\vartheta_{yl} = -1$, and when either of α and β keeps unchanged, the kirigami has the zero negative Poisson's ratio. The Poisson's ratio related to height change (see Supporting Note 1) and in-plane stiffness (see Supporting Note 2) of the proposed kirigami can be evaluated using similar analysis.

2.2. Material preparation

The kirigami patterns were fabricated from Kodak premium photo paper with dielectric constant and tangential loss of 2.85 and 0.05, respectively. Copper tape with conductivity of 5.8×10^7 Sm^{-1} was mounted on the bottom of the photo paper before cutting. Flat kirigami sheets have the dimension of 390 × 390 mm corresponding with 13 × 13 2D metamaterial unit cells and 845 2D meta-pixel, and complete folded structures (Mode II, III) have the dimensions of 130 × 130 mm.

2.3. Simulation

We performed numerical simulations using the ANSYS high frequency structure simulator (HFSS), a commercial finite-element analysis package. A unit cell with a master/slave boundary condition with Floquet port excitation is simulated as an infinite structure. We extracted reflection, S_{11}, and transmission, S_{21}, scattering coefficients for various polarizations, φ, and incident angles, θ; and calculated the absorptivity of the proposed structure is $A(\omega) = 1 - |S_{11}|^2 - |S_{21}|^2$. Furthermore, the induced electric, magnetic fields and surface current distribution of the absorbers are also presented by simulation.

2.4. Measurement

We experimentally verify the proposed kirigami absorption characteristic to compare with the simulation and calculation results. For accuracy, the 3D-printed frame was used to shape the prototypes of Mode II, III in to the desired complete folded angle. Transmission (S_{21}) and reflection (S_{11}) coefficients were measured using a WR-90 standard gain horn antenna with 15 dB nominal gain connected to Anritsu MS2038C vector network analyzer. For Mode I measurement, we used two antennas as transmitter and receiver, respectively; whereas for other modes we used a single antenna that simultaneously transmitted and received EM radiation. To keep geometric stability with the variable folding angle (α), Styrofoams with different width (g) are inserted between the metamaterial and 3D-printed frame (see Supporting Figure S7). The size of the 3D-printed frame is fixed at P = 139.1 mm which is the same size with 13 × 13 unitcell at

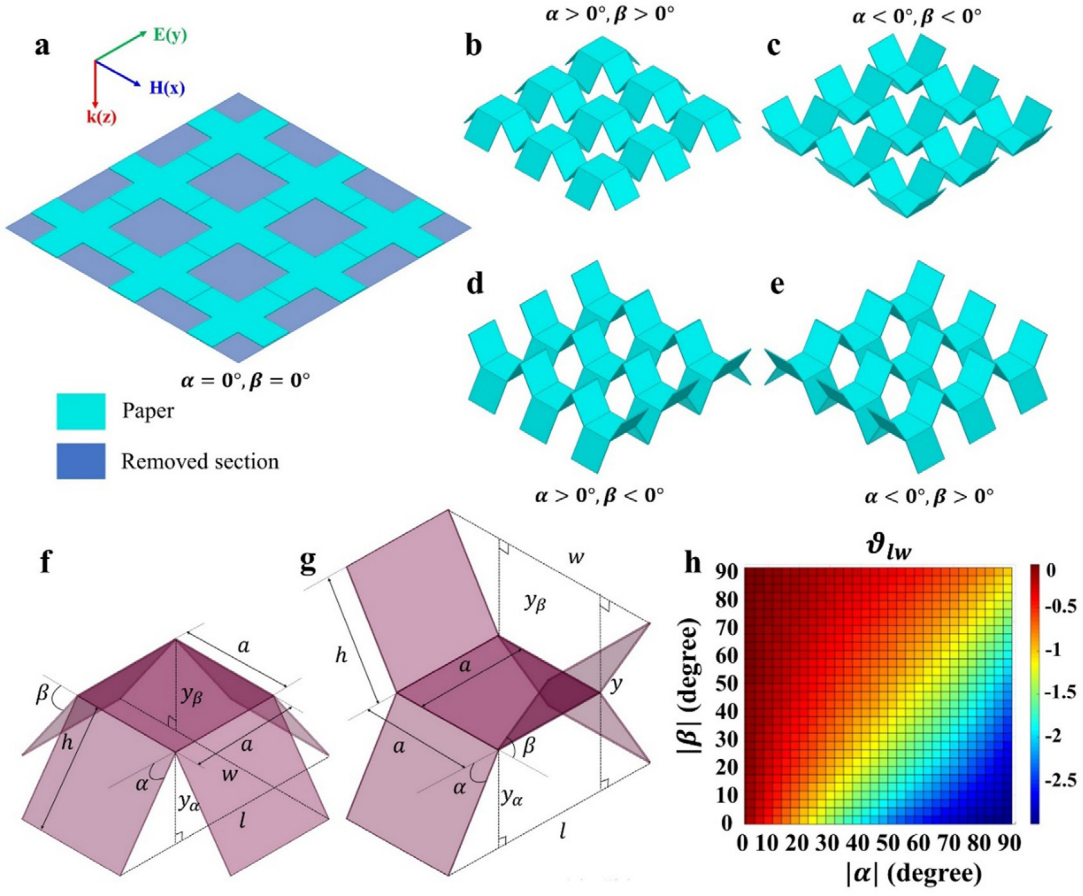

Fig. 2. Kirigami pattern geometries. (a) 3 × 3 cell array of kirigami pattern in unfolded state where α and β are the folding angles along y and x directions, respectively. (b–e) Four partial folded modes deduced from (a), corresponding to different value of α and β. The geometrical designed unit cell of f array in (b) and (c) (both α and β belong to range of [0°, 90°] or [0°, −90°]), (g) array in (d) and (e) (α and β belong to different ranges of [0°, 90°] and [0°, −90°]). (h) Linearized planar Poisson's ratio for all folded cases.

the folding angle of −88° . The corresponding g at the given α is calculated as:

$$g = \frac{P - 13a - 13 \cdot 2h \cdot \sin(90 - \alpha)}{2} \tag{3}$$

In this design, $P = 139.1$ mm, $a = 10$ mm, $h = 10$ mm and α is variable. For instance, when α is 88°, g is 0 mm. When α is increased to 90°, the Styrofoam with $g = 4.5$ mm is inserted between the metamaterial and 3D-printed frame.

3. Results and discussion

3.1. Multifunctional coding metamaterials

Fig. 3 shows the 2D unit cell kirigami patterns for Modes I–III, the proposed ternary coding, and the corresponding 3D metamaterial unit cells. The unit cell for each case has five 2D/3D meta-pixel elements. Ternary coded (−1, 0, +1) represent folded down, unfolded and folded up states, respectively. Since metamaterials have periodic arrangement, the unit-cell geometry has to satisfy x and y axis symmetry. Therefore, we propose five coding modes as shown.

- Mode I (Fig. 3b; $\alpha = \beta = 0°$), is the fundamental mode without folding where ternary code = 0 for all meta pixels.
- Mode II (Fig. 3c; $\alpha = \beta = -90°$) is coded as trit '0' at central meta-pixel and trit '+1' for all edge meta pixels.
- Mode III-1 (Fig. 3d; $\alpha = -90°$, $\beta = 90°$) and Mode III-2 (Fig. 3e; $\alpha = 90°$, $\beta = -90°$) are axisymmetric modes where the central meta-pixel is coded as trit '0' and two opposite edge meta-pixel pairs are coded as trit '−1' and '+1'.
- Mode III-3 (Fig. 3f; $\alpha = \beta = 90°$) is symmetric along the z-axis with Mode II, where the central meta-pixel is coded as trit '0' and four edge meta pixels are coded as trit '−1'.

The simulated results of transmission, reflection and absorption spectra for the proposed kirigami-based metamaterials are shown in Fig. 3g. Mode I acts as a band-pass filter with the center frequency of $f_1 = 8.75$ GHz. Mode II reflects all incident EM waves across the whole frequency range, i.e., operating as an EM reflector. Mode III provides perfect absorption at $f_0 = 4.3$ GHz. The absorption can be controlled by changing the folding state, providing absorption switching (ON and OFF states) and achieving 98% absorption when absorption mode was ON.

Polarization-selective metamaterials with manipulable characteristic have shown great advances for EM application. Normally, the polarization selection can be obtained by applying two complex external DC bias networks or using an asymmetric structures [41–44]. However, those structures can switch only between TE and TM polarization, whereas low performance at TEM polarization (see Table S1). By programming the folded states, three polarization-selectable characteristics of the Mode III are obtained, as illustrated in Fig. 3h–k. Under normal incident angle, Mode III-1 absorbs TE- while reflects TM-polarized waves, Mode III-2 the absorption for TE-polarized wave is blocked while be selected for TM-polarized wave, and Mode III-3 absorbs both TE and TM waves. This is due to resonance caused by the trapped EM wave being consumed in the folded down meta pixels

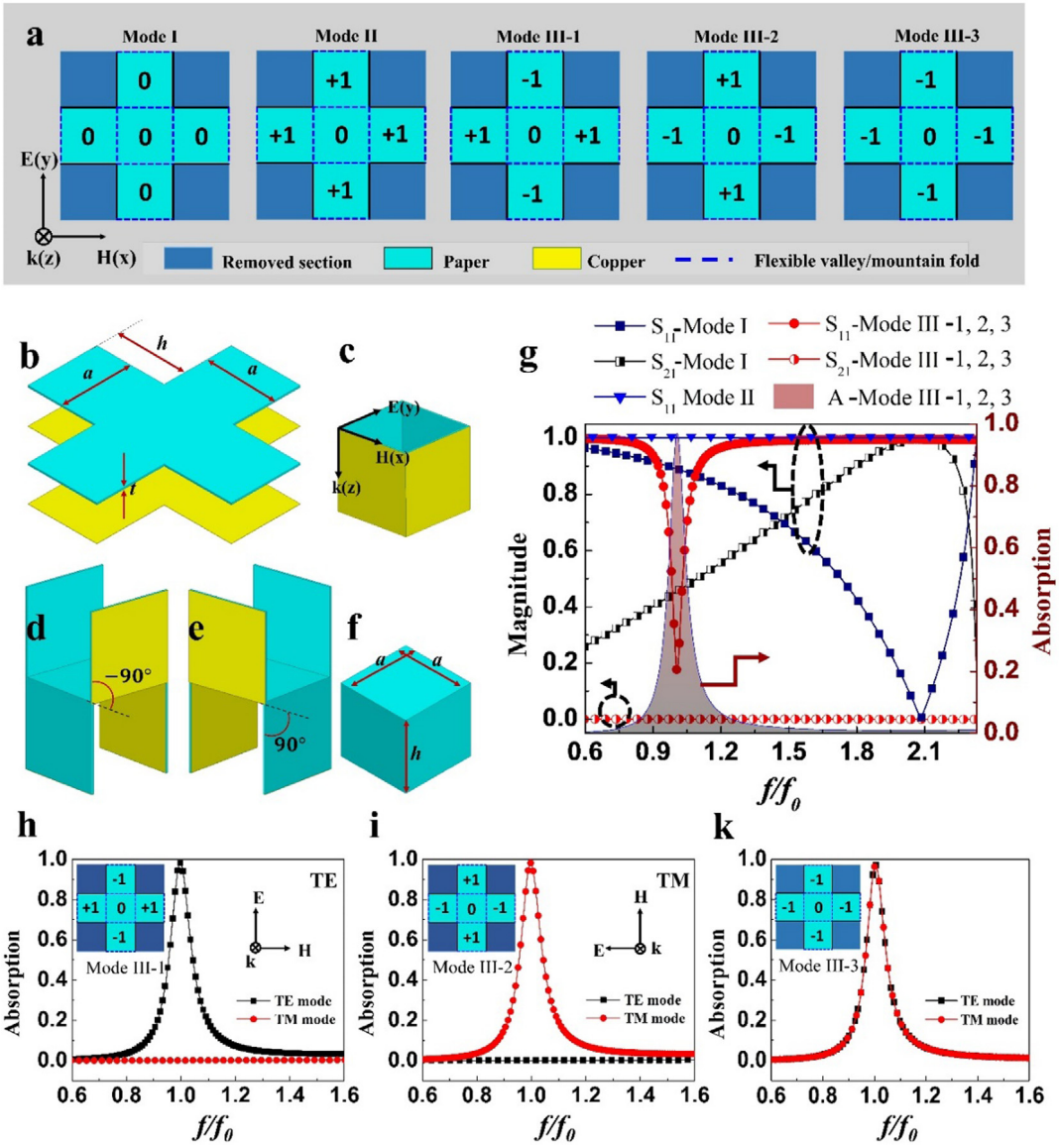

Fig. 3. Multifunctional coding metamaterials with corresponding unit cells and simulation results. (a) Multifunctional modes corresponding with five modes presented in Fig. 2a–e. Blue dashed lines indicate flexible valley–mountain folds. Ternary numerical code '−1', '0' and '+1' represent for three folding levels of each meta-pixel elements: Folded up, unfolded, folded down, respectively. (b) Bird-eye view of Mode I unit cell (unfolded state). (c–f) 3D view of kirigami unit-cell in full folded state (Mode II, III-1, III-2, III-3, respectively). (g) Scattering parameters and absorption characteristics of five-mode coding metamaterials. Simulated absorption of the proposed metamaterial at transverse electric (TE) and magnetic (TM) polarization for (h) Mode III-1, (i) Mode III-2, and (k) Mode-III-3. $t = 0.255$ mm, $h = 10$ mm, and $a = 10$ mm.

(see Supporting Note 3). The TE-polarized electric field is vertically perpendicular to the meta-pixel on the (y, z) plane, whereas while the TM-polarized electric field is vertically perpendicular to the meta-pixel on (x, z) plane. Therefore, the electric field for TE wave is trapped in Mode III-1, the electric field for TM wave is trapped in Mode III-2, the electric fields for both TE and TM waves are trapped in Mode III-3 leading to TE and TM polarization selection in three modes. Furthermore, the absorption characteristic is also investigated under wide range of polarization and incident angles to evaluate operational competency, as discussed in Supporting Note 5.

The absorbed EM power, P_{abs} can be theoretically expressed as:

$$P_{abs} = \frac{1}{2} 2\pi f \varepsilon'' |E|^2 , \tag{4}$$

where $|E|$ is the electric field magnitude and ε'' is imaginary components of the dielectric substrate. For conventional 3-layer (metallic–dielectric–metallic) metamaterial structures, the induced electric field is generally produced by resonance between the metallic parts under EM wave excitation. However, the proposed metamaterial comprises only two layers without an upper conductive pattern, hence there is no resonance and consequently no induced electric field and no absorption peak in the unfolded case (Mode I). Furthermore, The copper film on the bottom surface does not cover the whole area due to the cut out sections, hence, Mode I includes both transmission and reflection components (see Supporting Figure S3a). For all folded modes, there is no air gap among unit cells, hence, the copper film covers the whole area in back side, and consequently all transmission is blocked. Thus, all incident EM wave is reflected or absorbed, creating reflector and absorber metamaterials in Mode II, III (see Supporting Figure S3b and S3c). Since Mode II also lacks of resonator to generate resonance, similar to Mode I, there is no induced electric field, hence, it operates as an EM reflector.

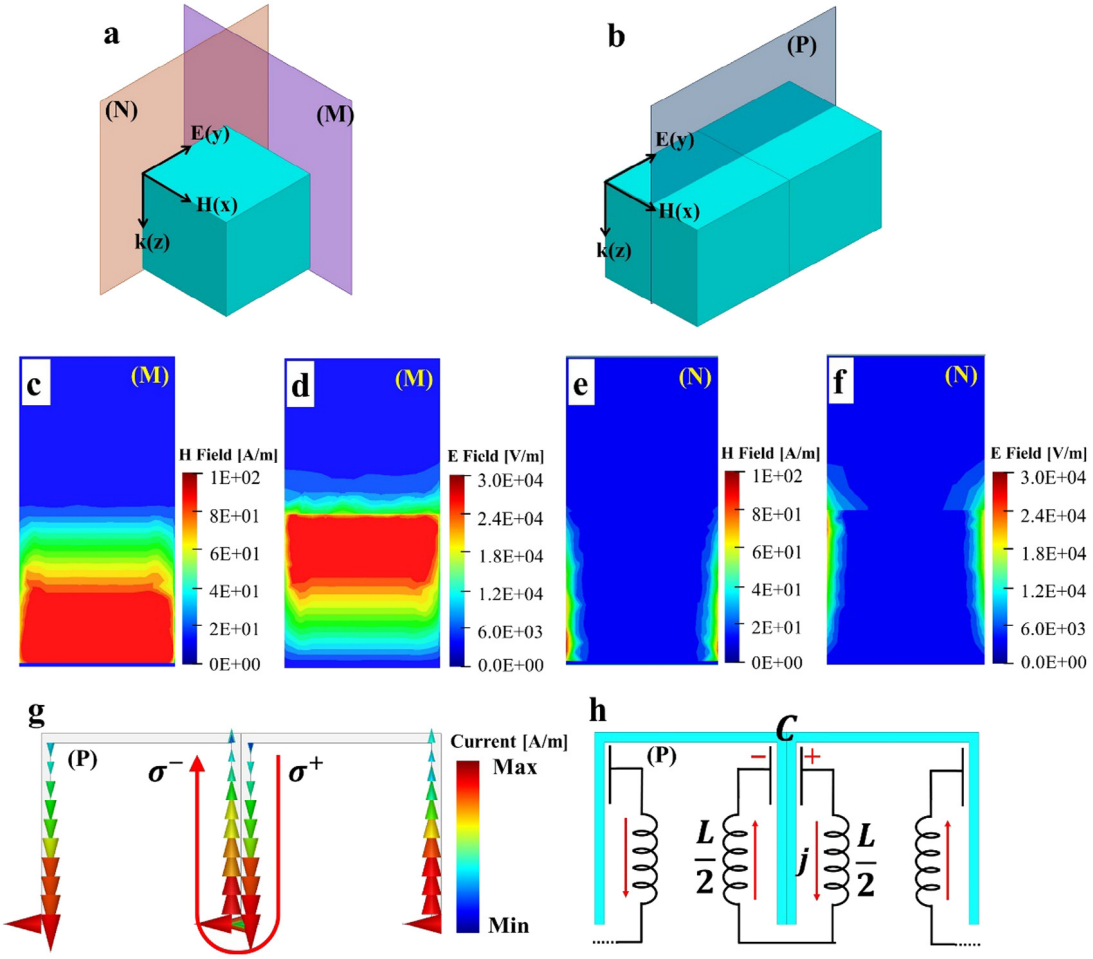

Fig. 4. Explanation for absorption peaks. (a) Mode III-3 unit cell with cutting-edge faces M, N, coplanar with (x, z) and (y, z) planes, respectively; (b) The diametral plane, P, for two adjacent unit cells along electric field vector. Induced (c), (e) magnetic and (d), (f) electric field distributions where (c), (d) corresponding to the plane M, and (e), (f) corresponding to plane N. (g) Current concentration and h equivalent LC circuit in plane P. The red arrows display current direction at investigated phase. σ^+ and σ^- denote surface charge density values.

To better understand the absorption characteristic for Mode III, we considered Mode III-3 only and numerically simulated the induced electric, magnetics fields and surface current distributions at resonance frequency in the M and N planes (see Fig. 4a), as exhibited in Fig. 4c–f. It can be seen that the induced electric and magnetic fields focus mostly on the top and the end of the folded sections, respectively. The induced fields contribute only in the M plane, perpendicular to vector E, and cannot be observed in the N plane, parallel to vector E. Therefore, the meta pixels along the y axis create the resonance by trapping the EM wave within the folded sections, leading to the absorption peak at 4.3 GHz. Fig. 4g shows anti-parallel current density accumulating on the copper film surface leading to the extracted equivalent LC circuit, as shown in Fig. 4h. The resonance frequency can be expressed as (see Supporting Note 3)

$$f_0 = \frac{1}{2\pi\sqrt{LC}} = \frac{c\sqrt{2}}{4\pi h\sqrt{c_1\varepsilon_2}} \tag{5}$$

where c is light speed, c_1 is numerical factor which is in range [0.2, 0.3] [45]. With the folding length $h = 10$ mm and the dielectric constant of paper $\varepsilon_2 = 2.85$, the absorption frequencies for Mode III is computed as 4.313 GHz, which is very similar to the simulation result (4.3 GHz).

3.2. Electromagnetic responses under different folding angles

The influence of folding angle on the absorption characteristic can be explain via Fig. 5. Fig. 5a exhibits the diametral cutting plane of two adjacent unit cell arranging on the y-axis. Fig. 5c illustrates the simulated absorption spectra for Mode III-3 working with various small folding angles ranged from 86° to 90°. The results indicate that absorptivity and resonance frequency of the kirigami absorber reduce rapidly with slight increase of folding angle. Detailly, simulated absorptivity reduced from 98% to 30% and simulated absorption peak increased from 4.3 GHz to 7.8 GHz by varying the folding angle from 90° to 86°, respectively. Detailly, we considered $\alpha = \beta$ for easier observation in this investigation.

The induced magnetic and electric field distributions observed in this plane are presented in Fig. 5d, e, where the induced fields focus mostly on the top and end regions of the folding section, respectively. An air gap appears in the folding sections when the kirigami pattern is not totally folded. The capacitance in Eq. (5) for a single unit cell can be express as (see Supporting Note S3):

$$C = \frac{\varepsilon_0\varepsilon_1\varepsilon_2 h c_1 a}{2\varepsilon_1 t + \varepsilon_2 h \sin(90^\circ - \alpha)} \tag{6}$$

where ε_0, ε_1 are permittivity of vacuum and the air, respectively. It is observed that the capacitance strongly depends on the folding angle, and the electric flux induced both in dielectric and

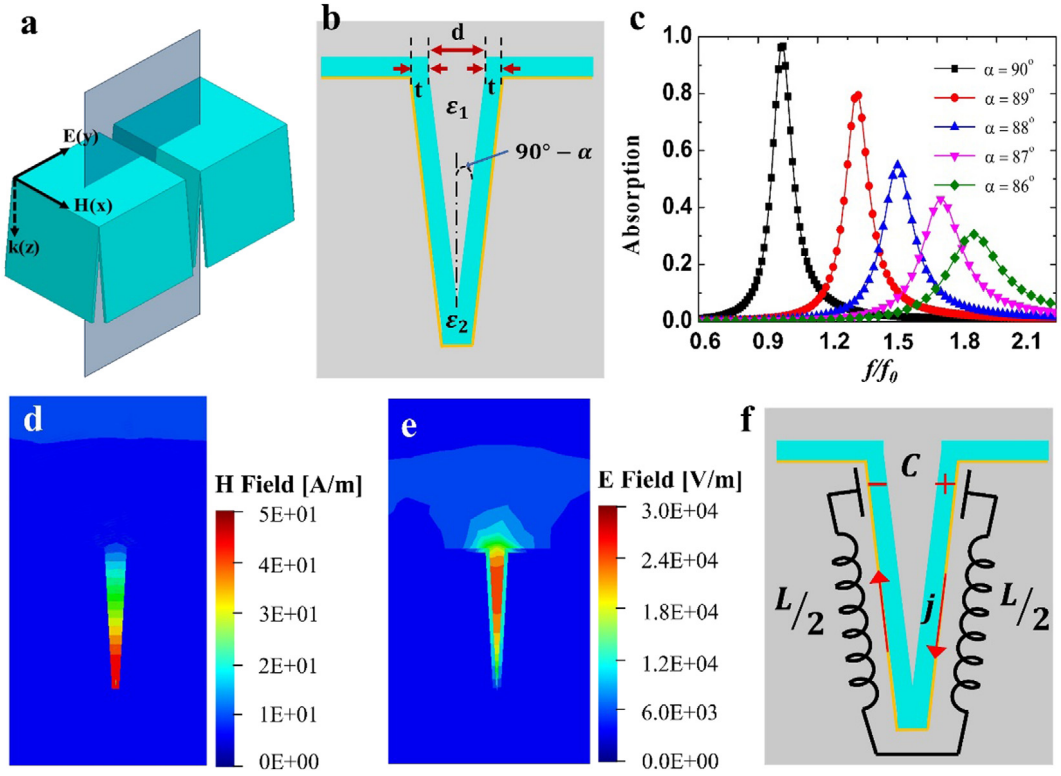

Fig. 5. Absorption frequency and ratio control according to minor changes of folding angle. (a) The diametral cutting plane for two adjacent unit cells with the folded angle of 87°; (b) geometry for the cutting plane from (a) (ε_1 and ε_2 are the permittivity of the air and paper substrate). (c) Simulated absorption spectra working with different folding angles. Induced d magnetic, e electric field distributions, and f equivalent LC circuit (red arrows display current density direction in the investigated phase) of the plane in (a).

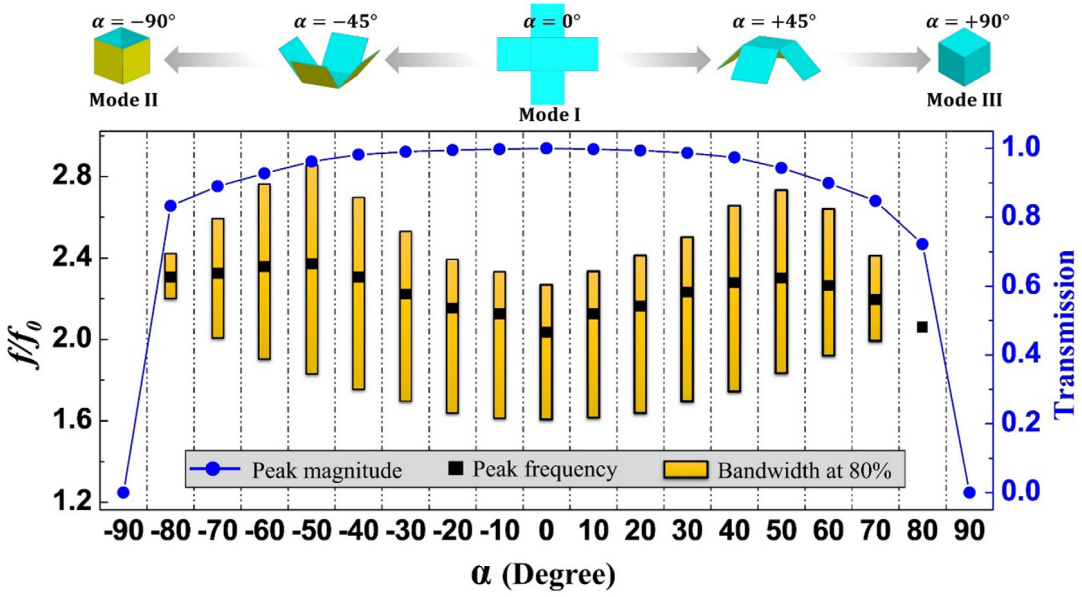

Fig. 6. Continuous tunable band-pass filter according to major changes of folding angle. Simulated band-pass responses of proposed kirigami structure, in which the bandwidths represent the magnitude of transmission coefficient cut off at 80%. The blue curve shows of transmission peak magnitudes, whereas black square dots exhibit transmission peak frequencies.

the air gap. Therefore, the capacitance decreases remarkably with reducing folding angle leading to resonance frequency shifting. Furthermore, when the folding angle is increased, the air gap in the (x, y) plane is broaden, increasing the transmission component, hence, reducing absorptivity. The influence of folding angles on absorption spectra caused by third-order magnetic resonance is discussed in Supporting Note 4 and Figure S4.

To clarify the band-pass properties, Fig. 6 presents the influence of various folding angles ranged from 0 (Mode I) to ±90 degree (Mode II and III) on transmission magnitudes and frequencies. It can be seen that the proposed kirigami structure can provide high transmission and its bandwidth can be continuously tuned by changing folding angle. Detaily, wide transmission bandwidth is realized from 6.9 to 12.27 GHz with transmissivity

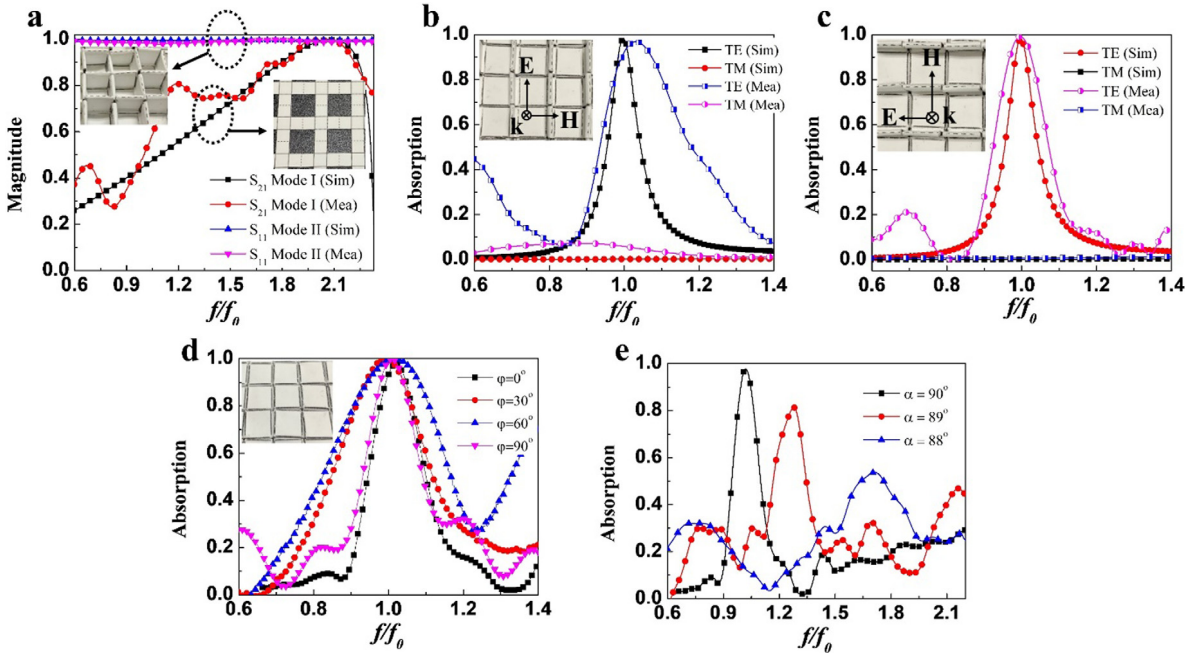

Fig. 7. Experimental verifications. Measured results for (a) Mode I and II, (b) Mode III-1, (c) Mode III-2 and (d), (e) Mode III-3 for various polarization and folding angles, respectively. (Inset: Optical images of actual mode tessellations).

higher than 80% when folding angles are stretched until $\alpha = 70°$ and $\alpha = -80°$. The transmission magnitude reduces when absolute values of folding angle increases and be blocked at fully folded states. It should be noted that the dielectric loss can be ignored due to thin paper thickness comparing with the operating frequencies. Therefore, the results for both $\alpha > 0°$ and $\alpha < 0°$ are almost similar. A little bit difference can be observed when $|\alpha| > 50°$ due to the high-order resonance which can be predicted by the third-order resonance in the case $\alpha > 50°$, as illustrated in Supporting Note 4. Here, we considered $\alpha = \beta$ for easier observation.

3.3. Experimental verification

The measured absorbance for Modes I-III are illustrated in Fig. 7. The measurement verifications showed good agreement with the simulation and calculation. It can be observed that, three kirigami absorbers resonate at 4.4 GHz in measurement, consistent with 4.3 GHz and 4.313 GHz in simulation and theoretical calculation. The slight differences between simulation and measurement arises from slight variations in folding angle, as discussed above. The measured absorptivity is higher than 95% (96%, 98%, and 97–98% for Modes III-1, III-2, III-3, respectively). For Mode III-3, we measure absorbance spectra working with various polarization angles (0°, 30°, 60°, and 90°) and three folding angles (90°, 89° and 88°) to compare with the simulation results shown in Figure S5a and Fig. 4c, respectively.

4. Conclusions

In summary, this paper numerically and experimentally investigated a programmable multifunctional metamaterial using a negative Poisson's ratio kirigami structure comprising dielectric paper and bottom conductor. We programmed the kirigami pattern using ternary coded folding states to transform from 2D meta-pixel to 3D meta-pixel structure, obtaining five functional modes.

- Mode I (unfolded) operated as a band-pass filter with center frequency $f_1 = 8.75$ GHz.
- Mode II operated as an EM reflector.
- Mode III resonated at $f_0 = 4.3$ GHz, providing perfect EM absorption and polarization selection.
    - Mode III-1 and III-2 provided TE- and TM-polarized wave selection modes, operating as ON and OFF states for normal incidence waves.
    - Mode III-3 absorbed both TE and TM waves, where absorptivity and resonance frequency were controllable by slightly changing the fold angle.

Moreover, the influence of folding angles on band-pass property and absorption characteristics at first- and third- order magnetic resonances are discussed in detail. The proposed kirigami metamaterial absorption performances were numerically simulated and experimentally verified.

Overall, numerous multifunctional electromagnetic metamaterials operating at various frequencies, switching by different techniques are qualitatively and quantitatively compared, as illustrated in Table S1. Our proposed structure has only two layers with transformable folding state, handling all common restrictions of high-cost, hi-tech, and difficulty in fabrication. Moreover, the proposed kirigami can be programmed by unique ternary code, therefore, it can provide more diverse functions, and promise wide range of application (see Supporting Note 7).

Declaration of competing interest

The authors declare that they have no known competing financial interests or personal relationships that could have appeared to influence the work reported in this paper.

CRediT authorship contribution statement

Dinh Hai Le: Conceptualization, Methodology, Data curation, Investigation, Formal analysis, Writing - original draft. **Ying Xu:** Formal analysis, Writing - review & editing, Validation. **Manos M. Tentzeris:** Supervision, Writing - review & editing, Validation. **Sungjoon Lim:** Funding acquisition, Methodology, Project administration, Supervision, Writing - review & editing.

Acknowledgments

This work was supported by the National Research Foundation of Korea (NRF) grant funded by the Korea government (MSIP) (No.2017R1A2B3003856).

Appendix A. Supplementary data

Supplementary material related to this article can be found online at https://doi.org/10.1016/j.eml.2020.100670.

References

[1] D.R. Smith, D.C. Vier, T. Koschny, C.M. Soukoulis, Electromagnetic parameter retrieval from inhomogeneous metamaterials, Phys. Rev. E 71 (2005) 1–11, http://dx.doi.org/10.1103/PhysRevE.71.036617.

[2] N. Kaina, F. Lemoult, M. Fink, G. Lerosey, Negative refractive index and acoustic superlens from multiple scattering in single negative metamaterials, Nature 525 (2015) 77–81, http://dx.doi.org/10.1038/nature14678.

[3] L. Liu, L. Wu, J. Zhang, Z. Li, B. Zhang, Y. Luo, Backward phase matching for second Harmonic generation in negative-index conformal surface plasmonic metamaterials, Adv. Sci. 5 (2018) 1800661, http://dx.doi.org/10.1002/advs.201800661.

[4] S.J. Kindness, N.W. Almond, B. Wei, R. Wallis, W. Michailow, V.S. Kamboj, P. Braeuninger-Weimer, S. Hofmann, H.E. Beere, D.A. Ritchie, R. Degl'Innocenti, Active control of electromagnetically induced transparency in a Terahertz metamaterial array with graphene for continuous resonance frequency tuning, Adv. Opt. Mater. 6 (2018) 1800570, http://dx.doi.org/10.1002/adom.201800570.

[5] X. Lu, M.A. Shapiro, I. Mastovsky, R.J. Temkin, M. Conde, J.G. Power, J. Shao, E.E. Wisniewski, C. Jing, Generation of high-power, reversed-Cherenkov wakefield radiation in a metamaterial structure, Phys. Rev. Lett. 122 (2019) 14801, http://dx.doi.org/10.1103/PhysRevLett.122.014801.

[6] H. Liu, Q. Zhang, K. Zhang, G. Hu, H. Duan, Designing 3D digital metamaterial for elastic waves: From elastic wave polarizer to vibration control, Adv. Sci. (2019) 1900401, http://dx.doi.org/10.1002/advs.201900401.

[7] H. Feng, M. Wang, L. Jiao, Z. Xu, X. Li, F. Xia, K. Zhang, W. Kong, L. Dong, M. Yun, Hase-coupled plasmon-induced transparency in metasurface with periodically arranged bimolecular systems, Appl. Surf. Sci. 506 (2020) 144888, http://dx.doi.org/10.1016/j.apsusc.2019.144888.

[8] L.D. Hai, V.D. Qui, N.H. Tung, T. Van Huynh, N.D. Dung, N.T. Binh, L.D. Tuyen, V.D. Lam, Conductive polymer for ultra-broadband, wide-angle, and polarization-insensitive metamaterial perfect absorber, Opt. Express 26 (2018) 33253–33262, http://dx.doi.org/10.1364/OE.26.033253.

[9] J. Li, C. Zhao, B. Liu, C. You, F. Chu, N. Tian, Y. Chen, S. Li, B. An, A. Cui, X. Zhang, H. Yan, D. Liu, Y. Zhang, Metamaterial grating-integrated graphene photodetector with broadband high responsivity, Appl. Surf. Sci. 473 (2019) 633–640, http://dx.doi.org/10.1016/j.apsusc.2018.12.194.

[10] C.T. Riley, J.S.T. Smalley, J.R.J. Brodie, Y. Fainman, D.J. Sirbuly, Z. Liu, Near-perfect broadband absorption from hyperbolic metamaterial nanoparticles, Proc. Natl. Acad. Sci. 114 (2017) 1264–1268, http://dx.doi.org/10.1073/pnas.1613081114.

[11] K. Chen, T.D. Dao, S. Ishii, M. Aono, T. Nagao, Infrared aluminum metamaterial perfect absorbers for plasmon-enhanced infrared spectroscopy, Adv. Funct. Mater. 25 (2015) 6637–6643, http://dx.doi.org/10.1002/adfm.201501151.

[12] H. Zhou, C. Yang, D. Hu, S. Dou, X. Hui, F. Zhang, C. Chen, M. Chen, Y. Yang, X. Mu, Integrating a microwave resonator and a microchannel with an immunochromatographic strip for stable and quantitative biodetection, ACS Appl. Mater. Interfaces 11 (2019) 14630–14639, http://dx.doi.org/10.1021/acsami.9b02087.

[13] D. Liu, L. Wang, Q. Cui, L.J. Guo, Planar metasurfaces enable high-efficiency colored perovskite solar cells, Adv. Sci. 5 (2018) 1800836, http://dx.doi.org/10.1002/advs.201800836.

[14] D. Hasan, C. Lee, Hybrid metamaterial absorber platform for sensing of CO2 gas at mid-IR, Adv. Sci. 5 (2018) 1700581, http://dx.doi.org/10.1002/advs.201700581.

[15] E. Jin, I.S. Lee, D. Kim, H. Lee, W.-D. Jang, M.S. Lah, S.K. Min, W. Choe, Metal–organic framework based on hinged cube tessellation as transformable mechanical metamaterial, Sci. Adv. 5 (2019) e4119, http://dx.doi.org/10.1126/sciadv.aav4119.

[16] X. Liang, A.J. Crosby, Uniaxial stretching mechanics of cellular flexible metamaterials, Extreme Mech. Lett. (2020) 100637, http://dx.doi.org/10.1016/j.eml.2020.100637.

[17] T.J. Cui, M.Q. Qi, X. Wan, J. Zhao, Q. Cheng, K.T. Lee, J.Y. Lee, S. Seo, L.J. Guo, Z. Zhang, Z. You, D. Chu, Coding metamaterials, digital metamaterials and programmable metamaterials, Light Sci. Appl. 3 (2014) e218, http://dx.doi.org/10.1038/lsa.2014.99.

[18] L. Zhang, X.Q. Chen, S. Liu, Q. Zhang, J. Zhao, J.Y. Dai, G.D. Bai, X. Wan, Q. Cheng, G. Castaldi, V. Galdi, T.J. Cui, Space–time-coding digital metasurfaces, Nature Commun. 9 (2018) 4334, http://dx.doi.org/10.1038/s41467-018-06802-0.

[19] Q. Ma, G.D. Bai, H.B. Jing, C. Yang, L. Li, T.J. Cui, Smart metasurface with self-adaptively reprogrammable functions, Light: Sci. Appl. 8 (2019) 98, http://dx.doi.org/10.1038/s41377-019-0205-3.

[20] L. Zhang, X.Q. Chen, R.W. Shao, J.Y. Dai, Q. Cheng, G. Castaldi, V. Galdi, T.J. Cui, Breaking reciprocity with space-time-coding digital metasurfaces, Adv. Mater. 31 (41) (2019) 1904069, http://dx.doi.org/10.1002/adma.201904069.

[21] S. Khan, T.F. Eibert, A multifunctional metamaterial-based dual-band isotropic frequency-selective surface, IEEE Trans. Antennas Propag. 66 (2018) 4042–4051, http://dx.doi.org/10.1109/TAP.2018.2835667.

[22] O. Balci, N. Kakenov, E. Karademir, S. Balci, S. Cakmakyapan, E.O. Polat, H. Caglayan, E. Özbay, C. Kocabas, Electrically switchable metadevices via graphene, Sci. Adv. 4 (2018) 1749, http://dx.doi.org/10.1126/sciadv.aao1749.

[23] R. Phon, S. Ghosh, S. Lim, Novel multifunctional reconfigurable active frequency selective surface, IEEE Trans. Antennas Propag. 67 (2019) 1709–1718, http://dx.doi.org/10.1109/TAP.2018.2889002.

[24] F. Zhang, S. Feng, K. Qiu, Z. Liu, Y. Fan, W. Zhang, Q. Zhao, J. Zhou, Mechanically stretchable and tunable metamaterial absorber, Appl. Phys. Lett. 106 (2015) 091907, http://dx.doi.org/10.1063/1.4914502.

[25] A. Shanian, F.X. Jette, M. Salehii, M.Q. Pham, M. Schaenzer, G. Bourgeois, K. Bertoldi, A. Gross, F. Javid, D. Backman, S. Yandt, M. Gerendas, T. Meis, K. Knobloch, F. Bake, D. Peitsch, Application of multifunctional mechanical metamaterials, Adv. Eng. Mater. 21 (2019) 1900084, http://dx.doi.org/10.1002/adem.201900084.

[26] J.Y. Ou, E. Plum, L. Jiang, N.I. Zheludev, Reconfigurable photonic metamaterials, Nano Lett. 11 (2011) 2142–2144, http://dx.doi.org/10.1021/nl200791r.

[27] J. Valente, E. Plum, I.J. Youngs, N.I. Zheludev, Nano- and micro-auxetic plasmonic materials, Adv. Mater. 28 (2016) 5176–5180, http://dx.doi.org/10.1002/adma.201600088.

[28] T. Kan, A. Isozaki, N. Kanda, N. Nemoto, K. Konishi, H. Takahashi, M. Kuwata-Gonokami, K. Matsumoto, I. Shimoyama, Enantiomeric switching of chiral metamaterial for terahertz polarization modulation employing vertically deformable MEMS spirals, Nature Commun. 6 (2015) 8422, http://dx.doi.org/10.1038/ncomms9422.

[29] P. Bhovad, J. Kaufmann, S. Li, Peristaltic locomotion without digital controllers: Exploiting multi-stability in origami to coordinate robotic motion, Extreme Mech. Lett. 32 (2019) 100552, http://dx.doi.org/10.1016/j.eml.2019.100552.

[30] S. Li, H. Fang, S. Sadeghi, P. Bhovad, K.W. Wang, Architected origami materials: How folding creates sophisticated mechanical properties, Adv. Mater. 31 (2019) 1805282, http://dx.doi.org/10.1002/adma.201805282.

[31] P.P. Pratapa, P. Suryanarayana, G.H. Paulino, Bloch wave framework for structures with nonlocal interactions: Application to the design of origami acoustic metamaterials, J. Mech. Phys. Solids 118 (2018) 115–132, http://dx.doi.org/10.1016/j.jmps.2018.05.012.

[32] Z. Wang, L. Jing, K. Yao, Y. Yang, B. Zheng, C.M. Soukoulis, H. Chen, Y. Liu, Origami-based reconfigurable metamaterials for tunable chirality, Adv. Mater. 29 (2017) 1700412, http://dx.doi.org/10.1002/adma.201700412.

[33] S.A. Nauroze, L.S. Novelino, M.M. Tentzeris, G.H. Paulino, Continuous-range tunable multilayer frequency-selective surfaces using origami and inkjet printing, Proc. Natl. Acad. Sci. USA 115 (2018) 13210–13215, http://dx.doi.org/10.1073/pnas.1812486115.

[34] R. Zhu, H. Yasuda, G.L. Huang, J.K. Yang, Kirigami-based elastic metamaterials with anisotropic mass density for subwavelength flexural wave control, Sci. Rep. 8 (2018) 483, http://dx.doi.org/10.1038/s41598-017-18864-z.

[35] L. Jing, Z. Wang, B. Zheng, H. Wang, Y. Yang, L. Shen, W. Yin, E. Li, H. Chen, Kirigami metamaterials for reconfigurable toroidal circular dichroism, NPG Asia Mater. 10 (2018) 888–898, http://dx.doi.org/10.1038/s41427-018-0082-x.

[36] G.K. Cuddalorepatta, W.M. van Rees, L. Han, D. Pantuso, L. Mahadevan, J.J. Vlassak, Poisson's ratio and residual strain of freestanding ultra-thin films, J. Mech. Phys. Solids 137 (2020) 103821, http://dx.doi.org/10.1016/j.jmps.2019.103821.

[37] Z. Hou, J. Zhang, P. Zhang, K. Wu, J. Li, Y. Wang, G. Liu, G. Zhang, J. Sun, Modulation-dependent deformation behavior and strengthening response in nanostructured Ti/Zr multilayers, Appl. Surf. Sci. 502 (2020) 144118, http://dx.doi.org/10.1016/j.apsusc.2019.144118.

[38] Y.-J. Lee, S.-M. Lim, S.-M. Yi, J.-H. Lee, S.-g. Kang, G.-M. Choi, H.N. Han, J.-Y. Sun, I.-S. Choi, Y.-C. Joo, Auxetic elastomers: Mechanically programmable meta-elastomers with an unusual Poisson's ratio overcome the gauge limit of a capacitive type strain sensor, Extreme Mech. Lett. 31 (2019) 100516, http://dx.doi.org/10.1016/j.eml.2019.100516.

[39] N. Easey, D. Chuprynyuk, W.M.S.W. Musa, A. Bangs, Y. Dobah, A. Shterenlikht, F. Scarpa, Dome-shape auxetic cellular metamaterials: Manufacturing, modeling, and testing, Front. Mater. 6 (2019) 1–13, http://dx.doi.org/10.3389/fmats.2019.00086.

[40] M. Lei, W. Hong, Z. Zhao, C. Hamel, M. Chen, H. Lu, H.J. Qi, 3D printing of auxetic metamaterials with digitally reprogrammable shape, ACS Appl. Mater. Interfaces 11 (2019) 22768–22776, http://dx.doi.org/10.1021/acsami.9b06081.

[41] H. Li, Q. Cao, Y. Wang, A novel 2-B multifunctional active frequency selective surface for LTE-2.1 GHz, IEEE Trans. Antennas Propag. 65 (2017) 3084–3092, http://dx.doi.org/10.1109/TAP.2017.2688927.

[42] H. Li, Q. Cao, L. Liu, Y. Wang, An improved multifunctional active frequency selective surface, IEEE Trans. Antennas Propag. 66 (2018) 1854–1862, http://dx.doi.org/10.1109/TAP.2018.2800727.

[43] Y. Zhang, L. Shi, D. Hu, S. Chen, S. Xie, Y. Lu, Y. Cao, Z. Zhu, L. Jin, B.O. Guan, S. Rogge, X. Li, Full-visible multifunctional aluminium metasurfaces by: In situ anisotropic thermoplasmonic laser printing, Nanoscale Horiz. 4 (2019) 601–609, http://dx.doi.org/10.1039/C9NH00003H.

[44] L. Peng, X. Li, X. Gao, X. Jiang, S. Li, Methodology for the design of a multifunctional device with switchable absorption and polarization conversion modes by graphene and metallic metasurfaces, Opt. Mater. Express 9 (2019) 687, http://dx.doi.org/10.1364/OME.9.000687.

[45] J. Zhou, E.N. Economon, T. Koschny, C.M. Soukoulis, Unifying approach to left-handed material design, Opt. Lett. 31 (2006) 3620, http://dx.doi.org/10.1364/OL.31.003620.